Mechanical Engineering and Materials Science
Independent Study

Mechanical Engineering & Materials Science

5-5-2023

Design and Characterization of 3D-printed Weaire-Phelan Hydrogel Lattices

Margrethe Ruding
Washington University in St. Louis

Follow this and additional works at: https://openscholarship.wustl.edu/mems500

Design and Characterization of 3D-printed Weaire-Phelan Hydrogel Lattices
by
Margrethe Ruding
Professor Philip Bayly

Washington University in St. Louis
St. Louis, Missouri
May 2023

1. Introduction[1]

Many fibrous, biological tissues, like white matter in the brain, are structurally and mechanically anisotropic (Feng et al., 2013; Bayly, 2014; Schmidt et al., 2018). Structural anisotropy refers to direction-dependent differences in the organization or orientation of tissue components. Mechanical anisotropy describes differences in the response of a material to loading in different directions. While mechanical anisotropy often accompanies structural anisotropy, they are not equivalent. Materials can be anisotropic in tension or shear, with corresponding tensile or shear moduli that describe their intrinsic stiffness. Mechanical properties of tissue may also change during human development, disease, or degeneration (Nanjappa and Kolipaka, 2014; Bayly, 2014).

Modeling soft tissue biomechanics is emerging as a tool to understand and prevent various disorders. One example is modeling traumatic brain injury (TBI), which is a significant contributor to mortality and morbidity among children and adults in the United States (Coronado et al., 2011). TBI is caused by high skull acceleration, often due to impact, which leads to tissue deformation followed by neuronal death, axonal disruption, and consequent loss of function, such as deficits in cognition or memory (Strich, 1956, 1961). Brain biomechanics models have been developed to elucidate the processes underlying TBI. Such models require accurate material properties of brain tissue (Ji et al., 2014; Kleiven and Hardy, 2002; Panzer et al., 2012; Alshareef et al., 2021). Similarly, material properties of muscle are needed for musculoskeletal simulations.

Magnetic resonance elastography (MRE) is a non-invasive technique that relies on MR imaging of shear waves to estimate mechanical properties (Muthupillai et al., 1995; Manduca et al., 2001). Tissue surrogate objects, or "phantoms," are often used to develop and evaluate magnetic resonance imaging (MRI) and image analysis procedures, including MRE. Soft gel (gelatin, agar, PDMS) phantoms have been used to simulate brain tissue for MRE studies (Kruse et al., 2008; Chatelin et al., 2013; Feng et al., 2022; Okamoto et al., 2011). Tissue-mimicking phantoms have been used in other biological tissue studies, such as the breast (Liney et al., 1999), muscle (de Merxem et al., 2017), and pelvic bone (de Bazelaire et al., 2004). However, with a few exceptions (Qin et al., 2013; Guidetti et al., 2019; Guertler et al., 2020; Schmidt et al., 2018) MRE phantoms have predominantly been isotropic. There is a pressing need for anisotropic phantoms with consistent, reproducible, tunable mechanical properties that can be characterized by simple mechanical tests for direct comparison with MRE.

Introducing anisotropy is particularly challenging in soft materials. A few recent studies have examined the use of anisotropic phantoms in MRE (Qin et al., 2013; Guidetti et al., 2019; Guidetti et al., 2021; Guertler et al., 2020; Smith et al., 2020; Schmidt et al., 2018). In the earliest studies,

---

it is unclear if anisotropy is introduced in both shear and tension/compression, how design changes would affect shear or Young's moduli, or how direct mechanical testing could verify properties.

Methods involving 3D-printing of biocompatible hydrogels can approximate organ geometry and tissue structure (Ramiah et al., 2020; Theus et al., 2020; Strobel et al., 2020). Hydrogels comprise a network of polymerized chains, allowing customization of biological and mechanical properties (Li et al., 2020). 3D-printing allows further customization of shape and structure. In principle, anisotropy may be introduced by a reinforcing fiber network or by lattice structures (Abate et al., 2020; Zheng et al., 2014). Previous work has characterized anisotropy in 3D-printed lattices (Egan et al., 2019; Abate et al., 2020) in materials greatly stiffer than soft tissue. Egan et al. (2019) reported a wide elastic modulus range between 16.3 and 155 MPa for lattice structures with four different unit-cell types.

Common 3D-printing methods used in bioprinting include ink-jet (Cui et al., 2012), extrusion (Hinton et al., 2015), laser-assisted (Guillotin et al., 2010), and stereolithography (SLA) (Guvendiren et al., 2016). The bio-ink used depends on the printing method and application (Bishop et al., 2017). Natural polymers include alginate, gelatin, and collagen. Synthetic polymers include gelatin methacrylate (gelMA), polyethylene glycol (PEG), and polyethylene glycol diacrylate (PEGDA). For this work, synthetic, pre-made PEGDA Start™ (CELLINK LLC, Boston, MA; Carlsbad, CA) photo-cured with the SLA printer LumenX+ (CELLINK) was used for low material cost, good fabrication accuracy, quick print time, and easy modification of physical and chemical parameters.

The objective of this work is to design, fabricate, and characterize scaled and unscaled 3D-printed hydrogel lattices with controlled structural and mechanical anisotropy. These 3D-printed hydrogel lattices could be used to create soft structures of desired shape and consistent mechanical properties for potential use as anisotropic tissue mimics. The topics in this report cover design techniques to generate 3D-modeled unit cell lattices using CAD software, fabrication using SLA, and experimental characterization by bench-top mechanical tests (uniaxial compression test).

2. Methods[2]

2.1 Lattice unit cell design

Samples were designed using the modeling software nToplogy (nTop inc., New York, NY). Unscaled and scaled versions of the Weaire-Phelan lattice was generated (Fig 1).

---

[2] This chapter closely follows previously-established procedures from Yoon, D., Ruding, M., Guertler, C. A., Okamoto, R. J., & Bayly, P. V. (2023). Design and characterization of 3-D printed hydrogel lattices with anisotropic mechanical properties. *Journal of the mechanical behavior of biomedical materials*, 138, 105652. https://doi.org/10.1016/j.jmbbm.2023.105652.

My contributions were designing and fabricating the lattice samples, performing uniaxial, unconfined-compression testing, analyzing the compression data, and co-authoring the paper with Daniel Yoon.
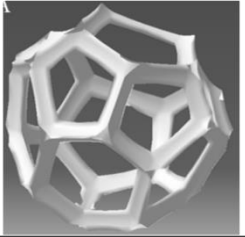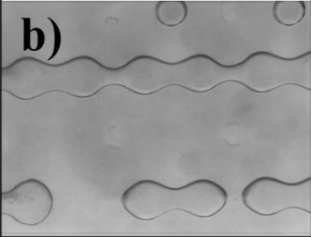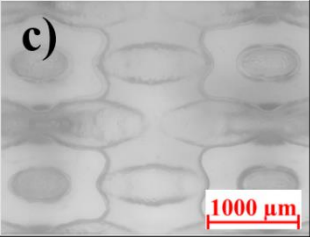
Figure 1. Unit-cell models and microscopic images of Weaire-Phelan lattices. (a) Representation of lattice unit cell. (b) Microscope photograph of the 3D-printed, unscaled lattice. (c) Microscope photograph of the 3D-printed, scaled lattice. [Microscope: ZEISS Axio Observer Z1m, Objective: 2.5x]

The unscaled lattice corresponds to a structure with the same parameters in all directions. The scaled lattice was generated such that the unit cell was scaled by a factor of two in the X-direction.

2.2 Fabrication

A LumenX + stereolithographic (SLA) bioprinter (CELLINK, Boston, MA) was used to 3D print samples (Fig. 2).
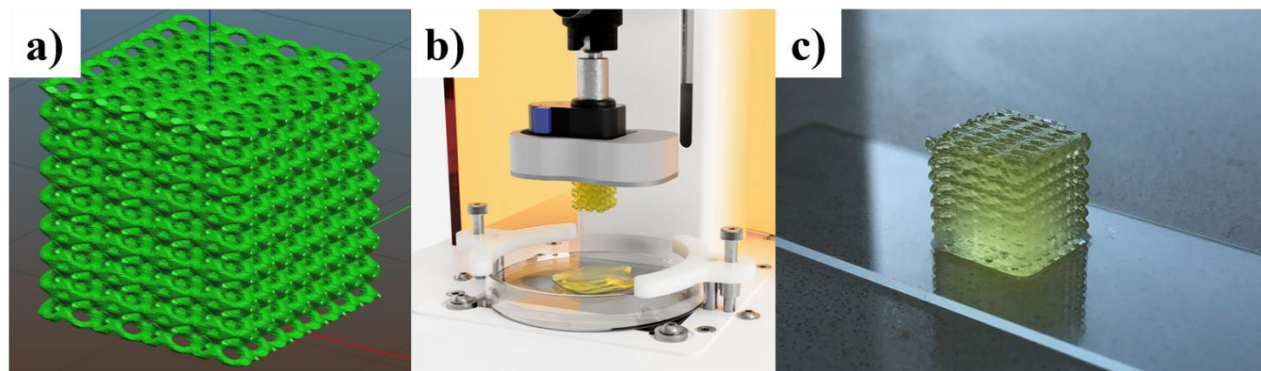

Fig 2. Fabrication process for a scaled lattice. The imaged lattice is composed of a vintile unit cell previously studied (Yoon, Ruding et al., 2023). (a) Representation of a 3D-rendered, scaled, vintile lattice exported as an .STL file. (b) The file is transferred to the LumenX+ bioprinter and the lattice is printed in PEGDA StartTM photo-ink; the print is cured via blue light projection. (c) Resulting scaled, vintile lattice.

PEGDA Start™ (polyethylene (glycol) diacrylate <2000 Da, CELLINK), a photocurable bioink, was cured with 100-µm layer resolution at a light intensity of 20 mW/cm^2. Each slice was illuminated for 5 s when in contact with the print bed; the first and last layers were illuminated for 25 s. Samples were printed using the Weaire-Phelan lattice structure in the unscaled and scaled configuration. Lattice cubes were nominally printed 10.00 mm in depth, width, and height (8 × 8 × 8 unit cells) for compression testing. The 3D-printed cube specimens (Fig. 3) included solid "wing" supports that extend 0.50 mm in height from the samples base and 2.45 mm beyond the sample to provide stability during printing.
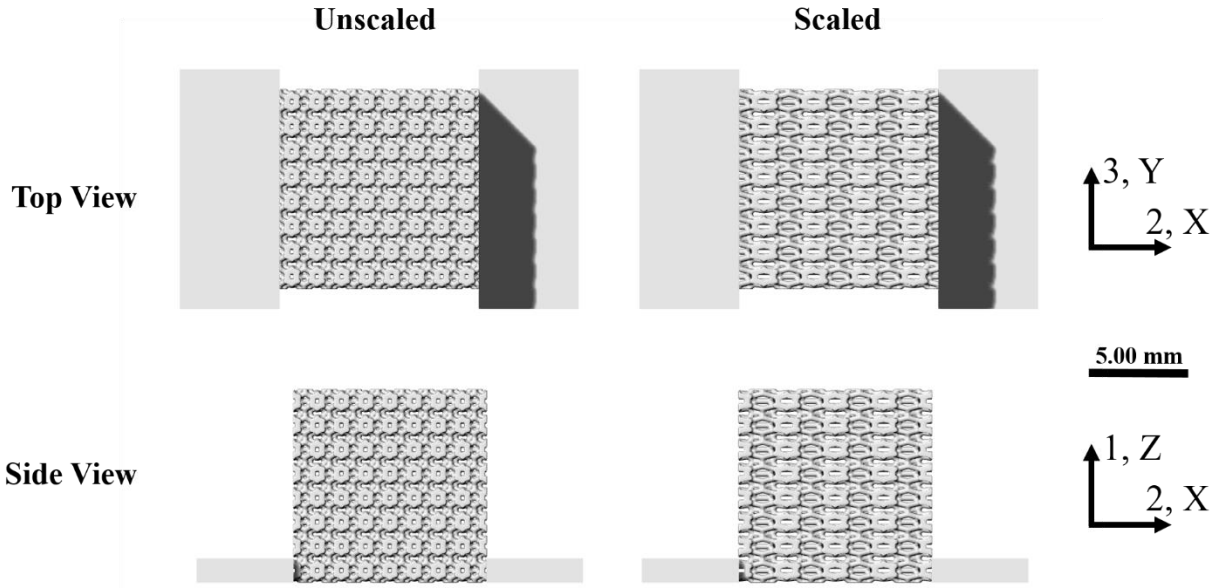
Figure 3. Unscaled and scaled Weaire-Phelan lattices for compression tests. (Top) Top view of unscaled and scaled lattices corresponding to the 2, 3- and X, Y-directions, respectively. (Bottom) Side view of unscaled and scaled lattices corresponding to the 2, 1- and X, Z-directions, respectively.

These "wings" were removed with a straight razor blade after printing. Once fabricated, samples were individually stored in DI water and placed in the refrigerator at $4°$ C to prevent dehydration and degradation. A total of 8 samples were created and used in this study: n = 4 for the unscaled and scaled cube lattices.

2.3 Uniaxial, unconfined compression testing

Each cube-shaped compression sample stored in DI water was removed from the refrigerator and allowed to equilibrate at room temperature (~23° C) for 30 minutes. For all tests, samples were submerged in DI water until testing. Samples were removed from DI water and tested on a rheometer (HR-20, TA Instruments, New Castle, DE) in compression mode (Fig. 4).
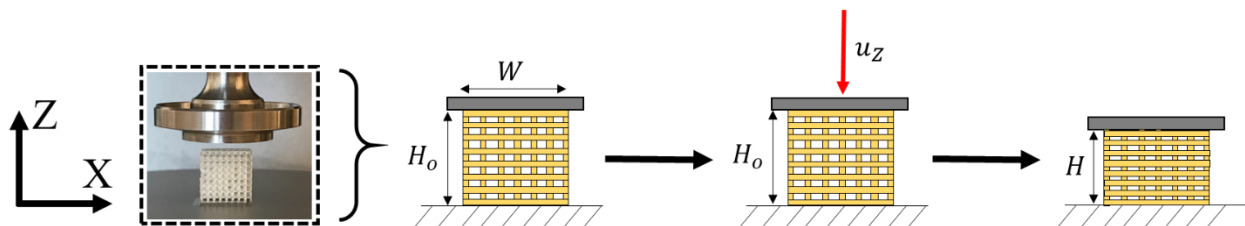
Figure 4. Schematic diagram of compression testing of a lattice structure. Cube-shaped sample undergoing simple uniaxial compression. The uncompressed cube sample is defined by its nominal sample height, H_o; the nominal area is the area of the entire, undeformed cube face: $A = W^2$. The depicted lattice is composed of a cubic unit cell previously studied (Yoon, Ruding et al., 2023).

The top platen (20 mm, flat) was lowered until contact was reached with an axial force of 0.05 N. A displacement ramp of 1 mm/min to 10% compression was then applied; axial load and displacement were recorded. Each cube-shaped sample was tested three times in different

directions. Scaled samples were compressed first in the build direction ("Z"), then in the scaled direction ("X"), and last in the non-build, unscaled direction ("Y"). Unscaled samples were tested in the same order, where "1" is the build direction, "2" is the unscaled, non-build direction with support wings, and "3" correspond to unscaled, non-build direction (Fig. 5). Testing of a single sample in all directions was completed within 15 minutes to minimize the effects of sample drying, and the sample was re-submerged between testing in different directions.
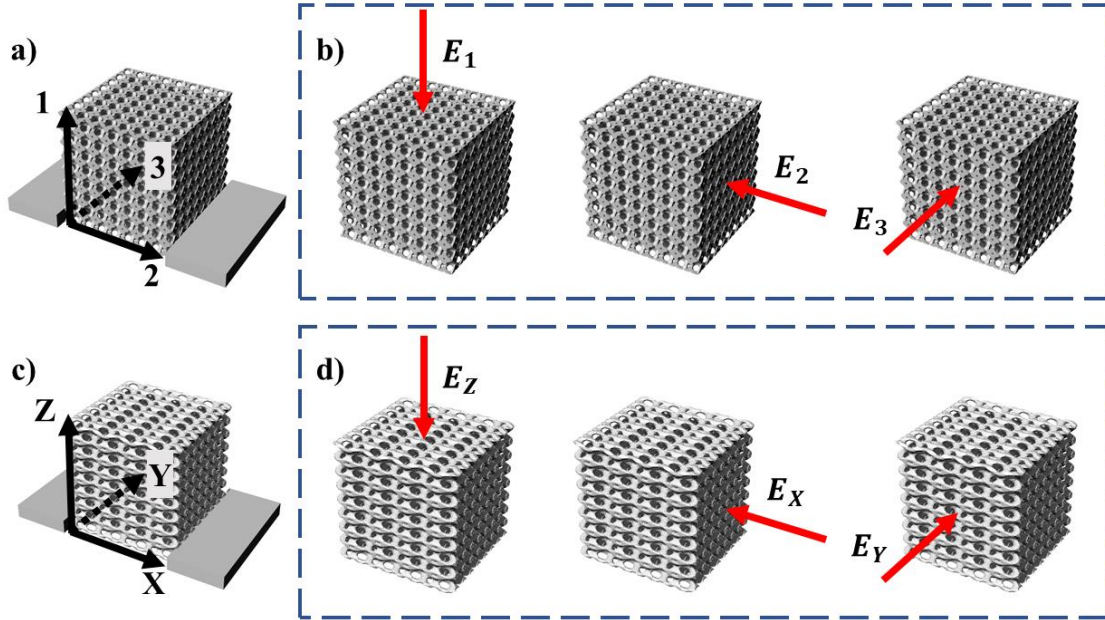

Figure 5. Schematic diagrams of scaled and unscaled 3D-printed lattices. The depicted lattice is composed of a vintile unit cell previously studied (Yoon, Ruding et al., 2023). (a) Numbered coordinate system used for unscaled lattices. (b) Unscaled vintile lattice depicting three loading directions and corresponding apparent Young's moduli – 1 (E_1), 2 (E_2), and 3 (E_3) (uniaxial displacement depicted by red arrow). (c) Standard X-Y-Z coordinate axis for scaled lattices. (d) Scaled vintile lattice depicting three loading directions and corresponding apparent Young's moduli – Z (E_Z), X (E_X), Y (E_Y) (uniaxial displacement depicted by red arrow).

2.4 Data analysis

Data, consisting of measured force and displacement values from compression tests, along with sample dimensions, was imported into the MATLAB environment (R2020a, MathWorks Inc., 2020) and analyzed using a custom script. The apparent Young's modulus in compression, E, (Eq. 2) was estimated from the slope of the stress-strain curve.

$$E = \frac{\bar{\sigma}}{\bar{\varepsilon}} = \frac{-F/A}{\Delta H/H} \qquad (2)$$

Nominal normal stress, $\bar{\sigma}$, was calculated from measured force, F, and the nominal surface area of the top face, A. Nominal strain, $\bar{\varepsilon}$, was measured from the displacement (change in height, ΔH) divided by the overall sample height, H. The specimen is allowed to expand laterally under compressive load, as in a standard unconfined compression test to estimate E. Using the approximations of linear elasticity, the not deformed area is used to estimate nominal stress. For scaled samples the apparent Young's modulus for loading in the build Z-direction is denoted as E_Z, in the scaled X-direction E_X, and in the unscaled Y-direction E_Y. For unscaled samples the apparent

Young's modulus for loading in the build Z-direction is denoted as E_1, the unscaled X-direction E_2, and the unscaled Y-direction E_3. While the hydrogel material is expected to be nearly incompressible, the lattice as a whole has voids that allow effectively compressible behavior.

2.5 Statistical analysis

Apparent Young's modulus

The null hypothesis is that loading direction (with respect to the lattice axes) has no effect on the apparent Young's modulus for a specific lattice type. To investigate this hypothesis, a one-way ANOVA multiple group comparison was conducted to compare the apparent moduli E_1, E_2, and E_3 in unscaled samples. The same ANOVA comparison was used to compare the apparent moduli E_X, E_Y, and E_Z in scaled samples. To determine if any differences between the three means was significant, a critical p-value, $\alpha = 0.05$, was used.

Ratios of apparent Young's moduli

The null hypothesis is that lattice scaling has no effect on the ratios of apparent Young's moduli for a specific lattice type. Un-paired t-tests were conducted to compare the ratio E_1/E_3 in unscaled samples to the ratio E_Z/E_Y in scaled samples, and to compare the ratio E_2/E_3 in unscaled samples to the ratio E_X/E_Y in scaled samples.

3. Results

Apparent Young's Moduli E_1 and E_2 recorded for unscaled Weaire-Phelan samples were roughly identical, while E_3 consistently exhibited the lowest value (Fig. 6). In scaled lattices, the apparent Young's modulus for loading in the scaled direction, E_X, was the highest while the non-build, unscaled E_Y and build, unscaled E_Z were similar. Numerical values of apparent Young's moduli and their ratios from compression experiments can be seen in Tables 1, 2. There is a significantly-high standard deviation for each test types, but a significantly-low standard deviation value for the ratio comparisons.
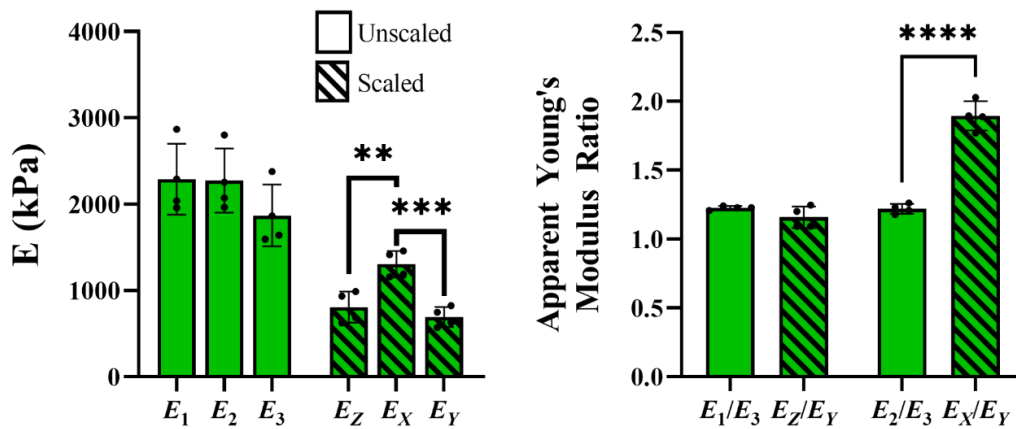

Figure 6. Apparent Young's modulus estimates and ratios from compression experiments. (a) Apparent Young's moduli in unscaled lattices (solid bars) and scaled lattices (crosshatched bars) for Weaire-Phelan lattices. *p<0.05 (significant); **p<0.01, ***p<0.001. (b) Ratios of apparent Young's moduli in unscaled lattices (solid bars) and scaled lattices (crosshatched bars).

Table 1. Apparent compressive moduli and ratios – unscaled lattices

	E_1 (kPa)		E_2 (kPa)		E_3 (kPa)		E_1/E_3		E_2/E_3	
	Mean	Std. Dev	Mean	Std. Dev	Mean	Std. Dev	Mean	Std. Dev	Mean	Std. Dev
Weaire-Phelan	2289	356	2274	322	1870	310	1.23	0.01	1.22	0.03

Table 2. Apparent compressive moduli and ratios – scaled lattices

	E_Z (kPa)		E_X (kPa)		E_Y (kPa)		E_Z/E_Y		E_X/E_Y	
	Mean	Std. Dev	Mean	Std. Dev	Mean	Std. Dev	Mean	Std. Dev	Mean	Std. Dev
Weaire-Phelan	808	156	1305	132	693	99	1.16	0.07	1.90	0.09

4. Discussion

Using PEGDA Start[TM], lattices composed of Weaire-Phelan unit cells were investigated by experiment to further our understanding of the effect of geometrical scaling on the mechanical behavior of 3D-printed hydrogel lattices. The elegant Weaire-Phelan unit cell is composed of two shapes, a pyritohedron and a tetrakaidecahedron, of equal volume and is known to have the smallest known surface area per cell since created in 1993 (Hao et al., 2021). When designed and fabricated with identical parameters, the Weaire-Phelan lattice demonstrated mechanical properties of approximately an order of magnitude larger than the cubic, diamond, and vintile lattices previously studied (Yoon, Ruding et al., 2023).

The behavior of the lattices in compression revealed effects of geometry and scaling, and the layer-by-layer resolution of the stereolithography printer, LumenX+. In the unscaled lattice a lower apparent Young's modulus was observed in the non-build direction without winged supports ($E_1 \approx E_2 > E_3$). When scaled, the lattices demonstrated a more transversely-isotropic behavior and became significantly less stiff with the highest observed value was in the scaled, non-build direction, E_X. This stiff behavior could be due to the printer's inability to fabricate the true design on the unscaled Weaire-Phelan lattice, thus leading to samples with a more solid structure than anticipated. As the design is scaled, it is likely that the printer is able to better replicate the design with larger porous regions. Geometrical scaling clearly introduces mechanical anisotropy in experimental samples, as seen when comparing E_X to E_Y and E_Z. Additionally, there is a significantly-large standard deviation for the values from each test type but a small standard deviation value for each ratio. This is potentially due to the inconsistencies of each print compared to one another, but an overall similar behavior in each test direction regardless of differing impurities.

5. Conclusion

Geometrically-scaled, 3D-printed, Weaire-Phelan, hydrogel lattices exhibited mechanical anisotropy in compression. The unit-cell type further proved that varying lattice type has a major impact on apparent Young's moduli. Additional examination of the Weaire-Phelan lattice with

increased resolution is necessary to understand the true behavior of the sample. Scaling in 3D-printed lattices is a powerful method to introduce mechanical anisotropy into soft-hydrogel materials for applications including MRE phantoms and engineered tissue surrogates.

References

Abate, K. M., Nazir, A., Yeh, Y., Chen, J., Jeng, J. (2020). Design, optimization, and validation of mechanical properties of different cellular structures for biomedical application. The international Journal of Advanced Manufacturing Technology, 106, 1253-1265, https://doi.org/10.1007/s00170-019-04671-5

Alshareef, A., Knutsen, A. Kl, Johnson, C. L., Carass, A. Upadhyay, K. (2021). Integrating material properties from magnetic resonance elastography into subject-specific computational models for the human brain. Brain Multiphysics, 2, 100038. https://doi.org/10.1016/j.brain.2021.100038.

Bayly, P. V., (2014). Magnetic Resonance Elastography of the Brain. Neu, C. P. & Genin, G. M. (Ed.1), Handbook of Imaging in Biological Mechanics (55-69). United Kingdom: Taylor and Francis

Bishop, E. S., Mostafa, S., Pakvasa, M., Luu, H. H., Lee, M. J., Wolf, J. M., Ameer, G. A., He, T., Reid, R. R. (2017). 3-D bioprinting technologies in tissue engineering and regenerative medicine: Current and future trends. Genes & Diseases, 4(4), 185-195, https://doi.org/10.1016/j.gendis.2017.10.002

Chatelin, S., Deck, C. & Willinger, R. (2013). An anisotropic viscous hyperelastic constitutive law for brain material finite-element modeling. Journal of Biorheology 27, 26–37 (2013). https://doi.org/10.1007/s12573-012-0055-6

Coronado, V. G., Xu, L., Basavaraju, S. V., McGuire, L. C., Wald, M. M., Faul, M. D., Guzman, B. R., Hemphill, J. D. (2011). Surveillance for Traumatic Brain Injury-Related Deaths – United States, 1997-2007 (No. 5). Centers for Disease Control and Prevention. https://www.cdc.gov/mmwr/pdf/ss/ss6005.pdf

Cui, X., Boland, T., D.D'Lima, D., Lotz, M. K. (2012). Thermal Inkjet Printing of Tissue Engineering and Regenerative Medicine. Recent patents on drug delivery & formulation, 6(2), 149–155. https://doi.org/10.2174/187221112800672949

de Bazelaire C. M.J., Duhamel, G. D., Rofsky, N. M., Alsop, D. C. (2004). MR imaging relaxation times of abdominal and pelvic tissues measured in vivo at 3.0 T: preliminary results. Radiology, 230(3) 652-9, https://doi: 10.1148/radiol.2303021331

de Merxem, A. G., Lechien, V., Thibault, T., Dasnoy, D., Macq, B. (2017). Design and implementation of a MRI compatible and dynamic phantom simulating the motion of a tumor in the liver under the breathing cycle. Proc. SPIE 10572: 13th International symposium on Medical Information Processing and Analysis, 10572, https://doi.org/10.1117/12.2285620

Egan, P., Wang, X., Greutert, H., Shea, K. Wuertz-Kozak, K., Ferguson, S. (2019). Mechanical

and Biological Characterization of 3D Printed Lattices. 3D Printing and Additive Manufacturing, 6(2), 73-81, https://doi.org/10.1089/3dp.2018.0125

Feng, Y., Okamoto, R. J., Namani, R., Genin, G. M., Bayly, P. V. (2013). Measurements of mechanical anisotropy in brain tissue and implications for transversely isotropic material models of white matter. Journal of the Mechanical Behavior of Biomedical Materials, 23, 117-132, https://doi.org/10.1016/j.jmbbm.2013.04.007

Feng, Y., Qiu, S. Chen, Y., Wang, R. He, Z., Kong, L., Chen, Y., Ma, S. (2022). Viscoelastic Characterization of Soft Tissue-Mimicking Gelatin Phantoms using Indentation and Magnetic Resonance Elastography. Journal of visualized experiments: JoVE, (183), 10.3791/63770. https://doi.org/10.3791/63770

Hao, M., Wei, C., Liu, X., Ge, Y., Cai, J. (2021) Quantitative evaluation on mechanical characterization of Ti6Al4V porous scaffold designed based on Weaire-Phelan structure via experimental and numerical analysis methods, Journal of Alloys and Compounds 885, doi: https://doi.org/10.1016/j.jallcom.2021.160234.

GraphPad Prism. (2020). Version 9.0.0 for Windows, GraphPad Software, San Diego, California USA, www.GraphPad.com

Guertler, C., Okamoto, R. J., Ireland, J. A., Pacia, C. P., Garbow, J. R., Chen, H., Bayly, P. V. (2020). Estimation of Anisotropic Material Properties of Soft Tissue by MRI of Ultrasound-Induced Shear Waves. Journal of Biomechanical Engineering, 142(3), https://doi.org/10.1115/1.4046127

Guidetti, M., Lorgna, G. Hammersly, M., Lewis, P., Klatt, D., Vena, P., Shah, R., Royston, T. J. (2019). Anisotropic composite material phantom to improve skeletal muscle characterization using magnetic resonance elastography. Journal of the Mechanical Behavior of Biomedical Materials. 89, 199-208, https://doi.org/10.1016/j.jmbbm.2018.09.032

Guidetti, M., Zampini, M. A., Jiang, Y., Gambacorta, C., Smejkal, J. P., Crutison, J., Pan, Y., Klatt, D., Royston, T. J. (2021). Axially – and torsionally-polarized radially converting shear wave MRE in an anisotropic phantom made via Embedded Direct Ink Writing. Journal of the Mechanical Behavior of Biomedical Materials. 119, 104483, https://doi.org/10.1016/j.jmbbm.2021.104483

Guillotin, B., Souquet, A., Catros, S., Duocastella, M., Pippenger, B., Bellance, S., Bareille, R., Rémy, M., Bordenave, L., Amédée, J., Guillemot, F. (2010). Laser assisted bioprinting of engineered tissue with high cell density and microscale organization. Biomaterials, 31(28), 7250–7256. https://doi.org/10.1016/j.biomaterials.2010.05.055

Guvendiren, M., Molde, J., Soares, R. M. D., Kohn, J. (2016). Designing Biomaterials for 3D Printing. ACS Biomaterials Science and Engineering, 2, 1679-1693. https://doi.org/10.1021/acsbiomaterials.6b00121

Hinton, T. J., Jallerat, Q., Palchesko, R. N., Park, J. H., Grodzicki, M. S., Shue, H-J., Ramadan, M. H., Hudson, A. R., Feinberg, A. W. (2015). Three-dimensional printing of complex biological structures by freeform reversible embedding of suspended hydrogels. Science Advances. 1(9), e1500758, https://doi.org/10.1126/sciadv.1500758

Ji, S., Zhao, W., Li, Z., McAllister, T. W. (2014). Head impact accelerations for brain strain-related responses in contact sports: a model-based investigation. Biomechanics and Modeling in Mechanobiology. 13, 1121-1136, https://doi.org/10.1007/s10237-014-0562-z

Kleiven, S., & Hardy, W. N. (2002). Correlation of an FE Model of the Human Head with Local Brain Motion--Consequences for Injury Prediction. Stapp car crash journal, 46, 123–144. https://doi.org/10.4271/2002-22-0007

Kruse, S. A., Rose, G. H., Glaser, K. J., Manduca, a., Felmlee, J. P., Jack Jr., C. R., Ehman, R. L. (2008). Magnetic resonance elastography of the brain. NeuroImage, 39(1), 231-237, https://doi.org/10.1016/j.neuroimage.2007.08.030

Li, J., Wu, C., Chu, P. K., Gelinksy, M. (2020). 3D printing of hydrogels: Rational design strategies and emerging biomedical applications. Materials Science and Engineering: R: Reports. 140, 100543, https://doi.org/10.1016/j.mser.2020.100543

Liney, G. P., Tozer, D. J., Turnbull, L. W. (1999). A Simple and Realistic Tissue-Equivalent Breast Phantom for MRI. Journal of Magnetic Resonance Imaging, 10, 968-971, https://doi.org/10.1002/(SICI)1522-2586(199912)10:6%3C968::AID-JMRI9%3E3.0.CO;2-0

MATLAB (2020). version 9.8.0.1380330 (R2020a). Natick Massachusetts: The MathWorks Inc.

Manduca, A., Oliphant, T. E., Dresner, M. A., Mahowald, J. L, Kruse, S. A., Amromin, E., Felmlee, J. P., Greenleaf, J. F., Ehman, R. L. (2001). Magnetic resonance elastography: Non-invasive mapping of tissue elasticity. Medical Image Analysis. 5, 237-254, https://doi.org/10.1016/S1361-8415(00)00039-6

Muthupillai, R., Lomas, D. J., Rossman, P. J., Greenleaf, J. F., Manduca, A., Ehman, R. L. (1995). Magnetic resonance elastography by direct visualization of propagating acoustic strain waves. Science, 269(5232), 1854-1857, https://doi.org/10.1126/science.7569924

Nanjappa, M. & Kolipaka, A. (2014). Magnetic Resonance Elastography of the Brain. Magnetic Resonance Imaging Clinics of North America, 22(3), 433-446, https://doi.org/10.1016/j.mric.2014.05.001

nToplogy (2022). New York, New York: nTop, Inc.

Okamoto, R. J., Clayton, E. H., Bayly, P. V. (2011). Viscoelastic properties of soft gels:

comparison of magnetic resonance elastography and dynamic shear testing in the shear wave regime. Physics in Medicine and Biology, 56(19), 6379-6400, https://doi.org/10.1088/0031-9155/56/19/014

Panzer, M., Myers, B. S., Capehard, B. P., Bass, C. R. (2012). Development of a Finite Element Model for Blast Brain Injury and the Effects of CSF Cavitation. Annals of Biomedical Engineering. 40(7), 1530-1544, https://doi.org/10.1007/s10439-012-0519-2

Qin, E. C., Sinkus, R. Geng, G., Cheng, S., Green, M., Rae, C. D., Bliston, L. E. (2013). Combining MR elastography and diffusion tensor imaging for the assessment of anisotropic mechanical properties: A phantom study. Journal of Magnetic Resonance Imaging. 37(1), 217-226, https://doi.org/10.1002/jmri.23797

R. R., (2021) Usage Protocol – PEGDA Start Photoink, CELLINK, Volumetric. https://www.cellink.com/wp-content/uploads/2019/11/2021-06-08_Usage-Protocol_PEGDA-Start-PhotoInk.pdf

Ramiah, P., du Toit, L. C., Choonara, Y. E., Kondiah, P. P. D., Pillay, V. (2020). Hydrogel-Based Bioinks for 3D Bioprinting in Tissue Regeneration. Frontiers in Materials. 7:76, https://doi.org/10.3389/fmats.2020.00076

Schmidt, J. L., Tweten, D. J., Badachhape, A. A., Reiter, A. J., Okamoto, R. J., Garbow, J. R., Bayly, P. V. (2018). Measurement of anisotropic mechanical properties in porcine brain white matter ex vivo using magnetic resonance elastography. Journal of the Mechanical Behavior of Biomedical Materials, 79, 30-37, https://doi.org/10.1016/j.jmbbm.2017.11.045

Smith, D. R., Guertler, C. A., Okamoto, R. J., Romano, A. J., Bayly, P. V., Johnson, C. L. (2020). Multi-Excitation Magnetic Resonance Elastography of the Brain: Wave Propagation in Anisotropic White Matter. Journal of biomechanical engineering, 142(7), 0710051–0710059. https://doi.org/10.1115/1.4046199

Strich, S. J. (1956). Diffuse Degeneration of the Cerebral White Matter in severe dementia following head injury. Journal of Neurology, Neurosurgery, & Psychiatry, 19(3), 163-185, https://doi.org/10.1136/jnnp.19.3.163

Strich, S. J. (1961). Shearing of NERVE FIBRES AS A CAUSE OF BRAIN DAMAGE DUE TO HEAD INJURY A Pathological Study of Twenty Cases, The Lancet, 444-448, https://doi.org/10.1016/S0140-6736(61)92426-6

Strobel, H. A., Moss, S. M., Hoying, J. B. (2020). Mechanical Considerations of Bioprinted Tissue. Frontiers in Mechanical Engineering, 6, https://doi.org/10.3389/fmech.2020.568726

Theus, A. S., Ning, L, Hwang, B., Gil, C., Chen, S., Wombwell, A., Mehta, R., Serpooshan, V.

(2020). Bioprintability: Physiomechanical and Biological Requirements of Materials for 3D Bioprinting Processes. Polymers, 12(10), 2262. https://doi.org/10.3390/polym12102262

Yoon, D., Ruding, M., Guertler, C. A., Okamoto, R. J., & Bayly, P. V. (2023). Design and characterization of 3-D printed hydrogel lattices with anisotropic mechanical properties. Journal of the mechanical behavior of biomedical materials, 138, 105652. https://doi.org/10.1016/j.jmbbm.2023.105652.

Zheng, X., Lee, H., Weisgraber, T. H., Shusteff, M., Deotte, J., Duoss, E. B., Kuntz, J. D., Biener, M. M., Ge, Q., Jackson, J. A., Kucheyev, S. O., Fang, N. X., Spadaccini, C. M. (2014). Ultralight, ultrastiff mechanical metamaterials, Science, 344(6190), 1373-1377, https://doi.org/10.1126/science.1252291